ELSEVIER

Contents lists available at ScienceDirect

Electrochimica Acta

journal homepage: www.journals.elsevier.com/electrochimica-acta



Electrode-supported high-tortuosity zeolite separator enabling fast-charging and dendrite-free lithium-ion/metal batteries

Kishen Rafiz, N.R.D. Harika, Jerry Y.S. Lin

School for Engineering of Matter, Transport and Energy, Arizona State University, Tempe, AZ 85287, USA

ARTICLE INFO

Keywords: Lithium-metal battery Plate-shaped zeolite Lithium dendrite Blade-coating Dendrite inhibition

ABSTRACT

Lithium-metal batteries (LMBs) are poised to be the next-generation high-energy density storage media of choice for various applications; however, they are currently plagued by failure due to dendrite propagation at high charge/discharge rates. One of the most sought-after technologies for dendrite propagation prevention in LMBs is solid state batteries, but they face commercialization challenges due to low room temperature ionic conductivity and high manufacturing cost. Here, we report the use of plate-shaped zeolite particles with intraparticle crystalline micropores to form an electrode-coated separator by a scalable blade-coating methodology. These separators with minimal polymer content are non-flammable and highly wettable to organic-based liquid electrolytes. They have high pore tortuosity and shear modulus resulting from the unique physical properties and morphology of the plate-shaped zeolite particles. LMB cells made of a LiNi_{0.5}Co_{0.2}Mn_{0.3}O₂ (NMC) cathode, $coated \ with \ the \ plate-shaped \ zeolite \ separator, \ LiPF_6-carbonate \ electrolyte, \ and \ lithium \ metal \ anode, \ show \ good$ charge-discharge characteristics and effectiveness in preventing dendrites from propagating through the separator even at high (3 C-rate) rates. When compared to LMB cells with a tortuously porous separator of similar pore size and porosity made of dense plate-shaped γ-alumina particles without intraparticle pores, cells with the zeolite separator show better charge/discharge characteristics, lower solid electrolyte interface (SEI) and chargetransfer resistances, and more effective dendrite propagation prevention. Results suggest that the intraparticle pores of the zeolite separator particles homogenize the Li-ion flux at the separator-anode interface in a much better manner than γ-alumina particles. There is promising commercial potential for the electrode-coated zeolite separator with highly tortuous pores for lithium batteries with a lithium-metal anode.

1. Introduction

Lithium-ion batteries (LIB) are presently the most widely used energy storage devices [1,2]. Lithium-metal batteries (LMB) with lithium as an anode are deemed the next-generation successor of the lithium-ion battery system due to their high theoretical specific capacity, potentially doubling that of LIB [3]. In LMBs, the lithium on the anode reacts vigorously with conventional organic electrolytes and salts to form a solid electrolyte interface (SEI). This SEI is not mechanically robust and breaks down on continuous cycling, thus again exposing the bare lithium metal, which further reacts with the electrolyte. This leads to a loss in capacity on continuous cycling of the cell [4]. Moreover, these areas where the SEI breaks down become points of high charge concentration, and lithium ions preferentially migrate to these defects to form dendrites. Thus, there is a non-uniform plating of lithium metal during further charging cycles [5]. On application of higher current

densities and subsequent charging/discharging, these dendrites pierce through the separator, causing an internal short circuit [6]. This can potentially lead to a thermal runaway reaction and a major fire/explosion hazard [7].

Commercial polymer separators currently being used are characterized by a low shear modulus and hardness, which makes them easily penetrable in case a lithium dendrite tries to propagate through them [8]. LMBs made with these polymer separators are particularly susceptible to penetration by the dendrites, especially at higher C-rates [9]. There have been several efforts to increase the shear modulus of the separator by embedding inorganic materials, such as silica and alumina, within the matrix of the polymer [10,11]. Also, inorganic materials have been coated on polymeric separators to increase their dendrite propagation prevention capability [12,13]. However, the properties of these inorganic modified polymer separators are still dominated by polymer. The effectiveness of the dendrite propagation prevention is achieved

E-mail address: Jerry.Lin@asu.edu (J.Y.S. Lin).

^{*} Corresponding author.

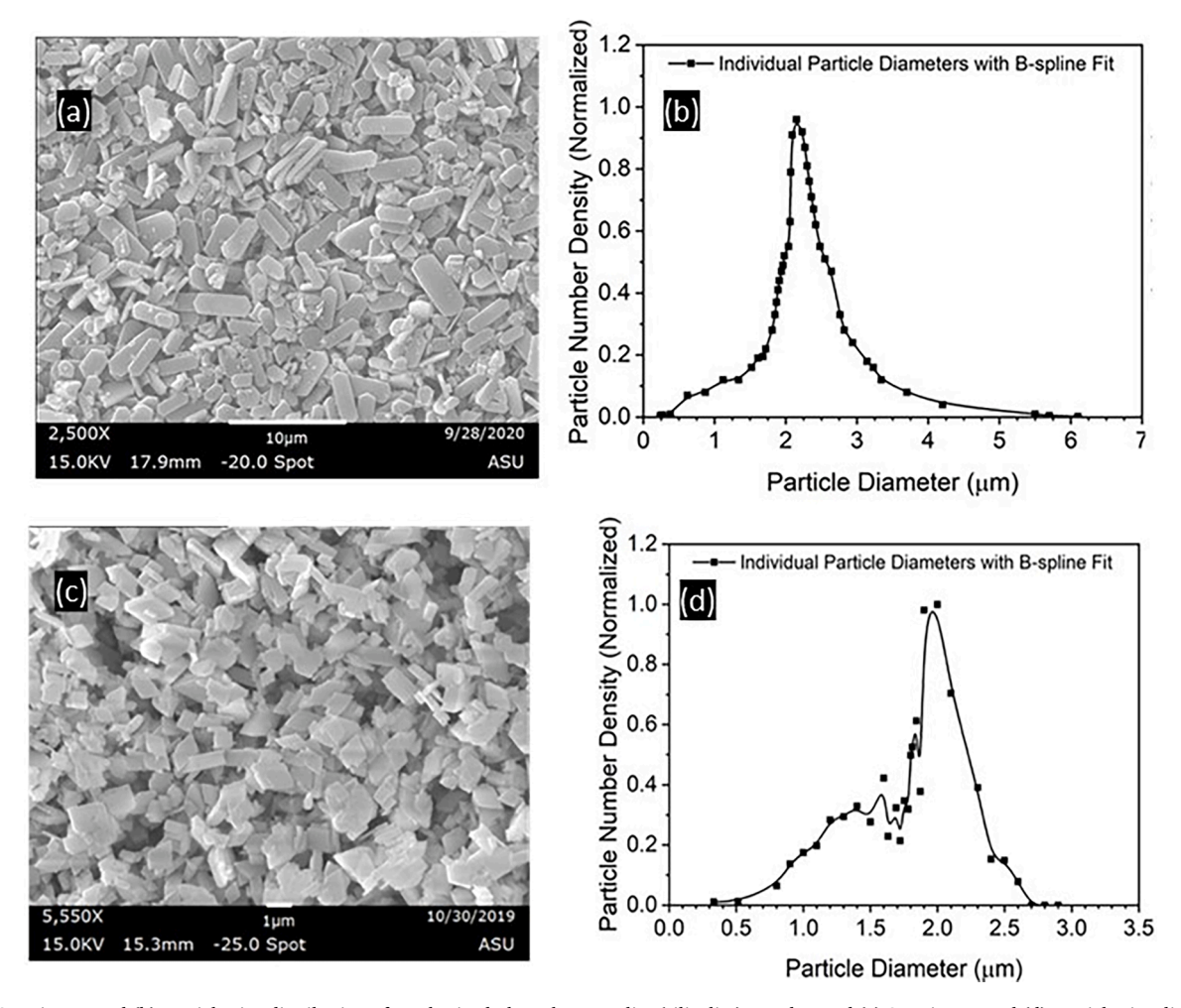


Fig. 1. (a) SEM image and (b) particle size distribution of synthesized plate-shape zeolite (silicalite) powder; and (c) SEM image and (d) particle size distribution of plate-shaped γ -alumina particles prepared in our lab and reported previously [31].

only at low rates of charge/discharge.

Another potent method of preventing dendrite propagation is the removal of the liquid phase electrolyte and polymeric separator, and replacement with a solid state electrolyte that has a high shear modulus [14]. The solid state electrolytes have been shown to work well in limiting dendrite propagation due to their rigid structure [15,16]. However, these electrolytes have lithium ionic conductivity an order of magnitude lower than the traditional liquid electrolytes at room temperature [17,18]. Also, they have an unstable interface with electrodes (especially Li anode), which leads to a loss in battery capacity upon continuous cycling [19,20].

One strategy to instill a high shear modulus to the separator without losing ionic conductivity at room temperature is to construct a separator matrix of ceramic particles which can take up the liquid electrolyte. This has been done by using anodic alumina [21], ZrO₂ [22], alumina [23], and silica [24]. However, these separators increase the weight-based density of the battery due to their high particle densities and do not provide a uniform distribution of lithium-ion flux at the separator-anode interface due to the dense nature of these particles. This absence of a uniform lithium-ion flux results in non-uniform plating of lithium on the anode [25], leading to excessive dendrite formation. Moreover, it was found that dendrites can still easily propagate through the pores of these porous ceramic separators at high C-rates of charge and discharge [26].

A promising strategy to prevent and inhibit high C-rate dendrite propagation is to use an inorganic separator with tortuous pores, such as one using modified silica particles [26] or silicon nanowires [27]. These separators are effective in inhibiting dendrite propagation only below a

2C-rate of charge and discharge. Hydroxyapatite (HAP) nano-wire separators with a high pore tortuosity have also been functional in reducing dendrite propagation at high current densities, but they are not stable at higher operating temperatures, above 55 °C, for more than 70 cycles [28]. Solid state electrolytes with enhanced solid-phase tortuosity (with pores in the electrolyte) offer improved dendrite propagation prevention at both low and high C-rates but are unable to function stably even at room temperature conditions [29]. Tortuously porous polybenzimidazole (PBI) membranes synthesized by a non-solvent method showed potential to reduce dendrite propagation due to a higher tortuosity, but they were limited to preventing this only at a low current density of 1 mAh cm⁻² [30].

The effectiveness of using separators with tortuous pores filled with a liquid electrolyte in inhibiting dendrite propagation was more clearly demonstrated in our recent work [31]. We compared the performance of $LiNi_{0.5}Co_{0.2}Mn_{0.3}O_2$ (NMC)/LiPF₆-carbonate/Li cells electrode-coated separators made of (1) plate-shaped γ -alumina particles with pore tortuosity of about 7.0 and (2) spherical α-alumina particles with pore tortuosity of 2.9. Both separators have similar pore sizes. The same cell using a conventional PP-2500 separator with a tortuosity of 2.3 was also studied for bench-mark purpose. Cells with the tortuously porous γ-alumina separator exhibited a marked improvement in terms of inhibiting dendrite propagation due to the greater tortuosity and hardness of the separator, as compared to the conventional PP-2500 and α-alumina separators. However, the separators made of the dense γ -alumina particles without intraparticle pores do not provide a uniform distribution of lithium-ion flux at the separator anode interface, which

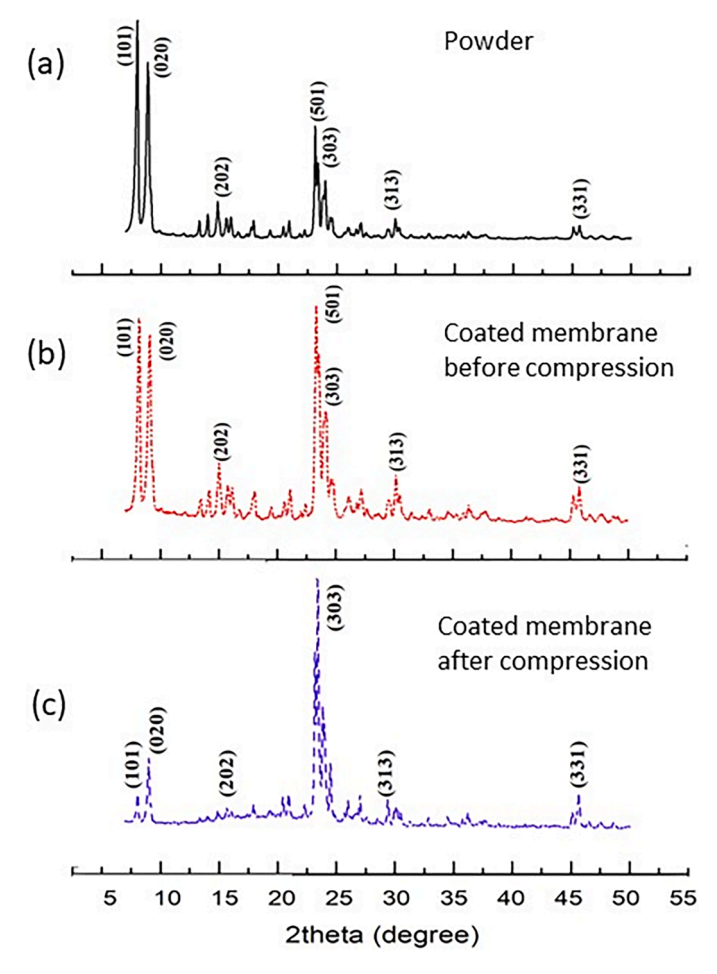


Fig. 2. XRD patterns of (a) synthesized silicalite powder; (b) silicalite membrane separator of 40 μ m thickness coated on the NMC electrode before compression; and (c) silicalite membrane separator of 40 μ m thick on the NMC electrode and compressed to 400 psi.

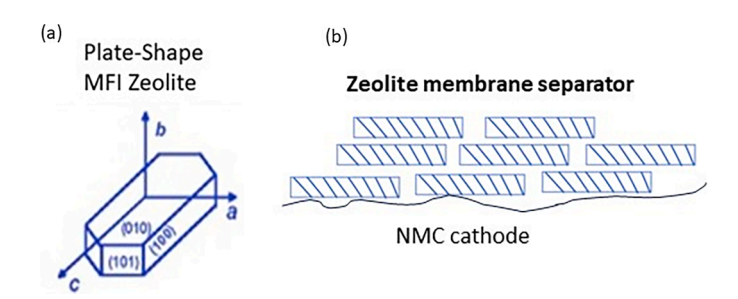
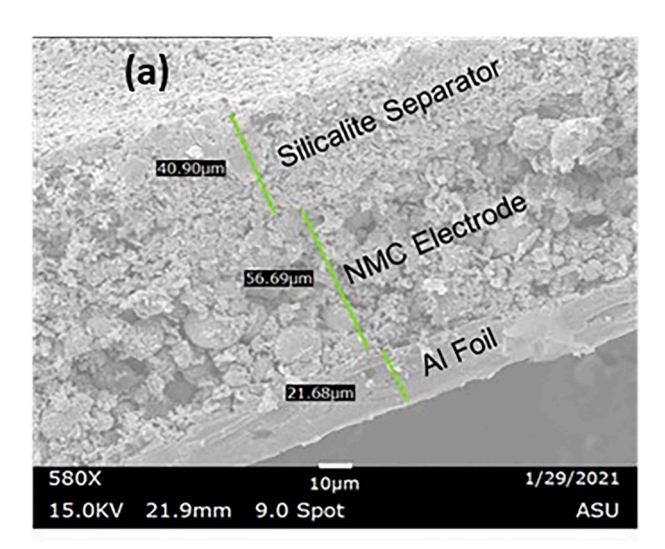


Fig. 3. Schematic illustration of (a) plate-shaped MFI zeolite crystal showing crystallographic planes and (b) structure of membrane separator made of plate-shaped zeolite on NMC cathode after compression.

results in non-uniform plating of lithium on the anode and higher SEI and charge-transfer resistance [31]. γ -alumina particles also have high particle density, lowering the weight-based energy density of the battery.

Recently, we discovered that LIBs of $LiNi_{0.5}Co_{0.2}Mn_{0.3}O_2$ (NMC)/ graphite with a separator made of microporous zeolite (pure silica MFI zeolite) particles with intraparticle crystalline pores and fire-safe, salt-concentrated electrolyte of lithium bis-fluoro sulphonyl imide (LiFSi) in tri-methyl phosphate solvent (TMP) 99.999% purity performed much better than the same batteries but with separator made of dense silica particles with the same geometries [32]. Compared to the dense silica



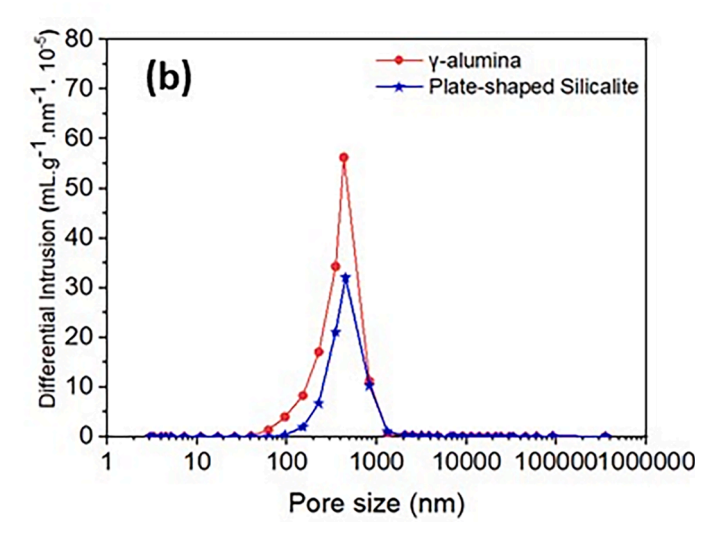


Fig. 4. (a) Cross-sectional SEM image of the plate-shaped zeolite separator coated on the NMC electrode; (b) Pore size distribution of zeolite (silicalite) membrane when coated as a 40 μ m thick separator on aluminum foil and the pore size distribution of γ -alumina membrane separator reported previously [31].

particles, the zeolite particles with intraparticle crystalline pores offer lower density and higher hydrophobicity, making it highly wettable for a LiFSi/TMP electrolyte. Furthermore, the intraparticle pores of microporous zeolite allow possible transport of lithium ions, which may contribute to the higher performance of the lithium-ion batteries with the salt-concentrated electrolyte. More recently, we found that lithium-ion batteries with zeolite separator of higher pore tortuosity (about 7) filled with LiFSi/TMP electrolyte performed better than the same lithium-ion batteries with the same zeolite having a low tortuosity (<3) [33]. The positive effect of high pore tortuosity demonstrated in the separator made with plate-shaped γ-alumina [31] and obvious advantages of low density, hydrophobicity, and availability of intraparticle pores of zeolite discovered in our recent work on lithium-ion batteries [32,33] prompted us to study the effectiveness of a separator made of plate-shaped zeolite particles with high interparticle pore tortuosity on the inhibition of dendrite formation and propagation in lithium-ion/metal batteries with a conventional liquid electrolyte. We report the results of this study here.

Table 1
Pore structure of zeolite and γ-alumina (both 40 um thick) and propylene (25 um thick) separators and resistances of lithium-ion battery cells with these separators.

Separator	Pore Radius (nm)	Interparticle Porosity (%)	Tortuosity (EIS Method)	Resistance in Circuit (Ohm/cm ²)		
				Rohmic	R _{SEI}	R _{charge-transfer}
Dense γ-alumina	~ 430	54	6.95	6.85	239	395
MFI zeolite	~450	50	6.31	6.99	221	363
PP2500	~65	39	2.32	3.14	179	301

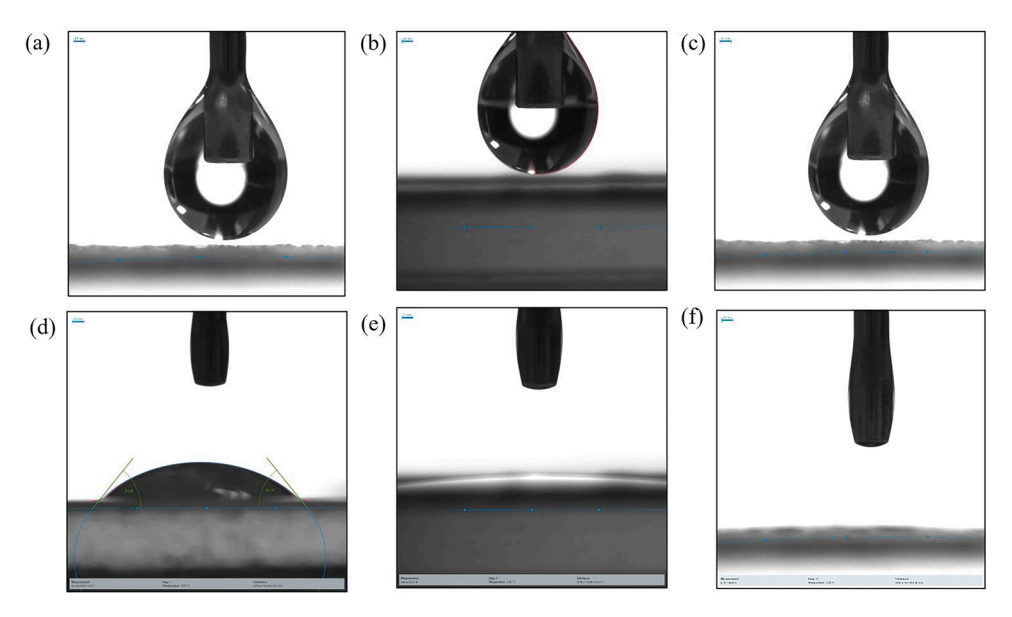


Fig. 5. Contact angle measurement results of LiPF₆-salt/carbonate-solvent electrolyte on separator surface: At t = 0 s, the electrolyte drop from the syringe against (a) PP separator (b) alumina separator (c) zeolite (silicalite) separator; At t = 1 s, the structure and contact angle of the drop on (d) PP separator (e) γ-alumina separator (f) zeolite (silicalite) separator.

2. Experimental

2.1. Synthesis of plate-shaped zeolite and preparation of the coating slurry

Plate-shaped pure silica MFI type zeolite (silicalite) particles were synthesized hydrothermally by modifying the method of Lu et al. [34]. A synthesis solution was prepared by mixing 10 g of tetraethyl orthosilicate (reagent grade, 98% by wt.; Aldrich), 4 g of tetrapropyl-ammonium hydroxide (1 M in H₂O; Sigma Aldrich), and 170 g of de-ionized water, stirred for 24 hrs. The obtained clear solution was transferred to an autoclave and heated in an oven at 155 $^{\circ}\text{C}$ for 10 h to obtain the required plate-shape zeolite particles. The autoclave was then cooled to room temperature, and zeolite powders were collected and dried at 120 °C in a vacuum chamber to remove any traces of moisture and calcined at 600 °C for 18 h in air to remove the organic template. For a coating separator, a zeolite slurry was prepared by mixing 3 g of powder with 1 g of 5 wt.% polyvinyl alcohol (PVA) aqueous solution (molecular weight: 77, 000-79,000 Da) (ICN Biomedical Inc., USA) and 1 g of de-ionized water. The slurry was stirred to the desired consistency and homogeneity with no air bubbles. This slurry was further ground using a mortar and pestle for ~ 10 mins by hand to smoothen it further.

2.2. Formation of the electrode-coated separator and its characterization

Lithium-metal chips (0.1 mm in thickness and 15.6 mm in diameter), a LiNi $_{0.5}$ Co $_{0.2}$ Mn $_{0.3}$ O $_{2}$ (NMC) cathode (45 μ m in thickness, with active mass loading of 121 g/m 2), 1 M LiPF $_{6}$ salt in equal volume of ethyl carbonate (EC), diethyl carbonate (DEC) and dimethyl carbonate (DMC) (with EC:DEC:DMC= 1:1:1, v/v/v) in a sealed container, were all procured from MTI, USA. To establish control-cell performance, a

commercial PP-2500 separator of 25 μm thickness was procured from Celgard LLC, USA, and used to make cells similar to those with the zeolite separator. The components for constructing the CR-2032 cells were procured from X2 Labwares, Singapore.

The slurry of plate-shaped zeolite powder described above was dropped across one of the edges of the substrate (NMC cathode and aluminum foil) and then spread down along the length of the substrate using a caliper-adjustable doctor blade (Gardco LLC, USA). The coating of the zeolite separator on the NMC cathode was for making coin NMC-Li cells and on aluminum foil for testing the conductivity of the zeolite separator filled with electrolyte or pore structure of the separator. To produce the electrode-supported zeolite separators, the initial blade gap was kept at $50 \, \mu m$. The coated zeolite separators were dried for $8 \, h$ in a humidity-controlled chamber at 40 $^{\circ}\text{C}$ and 60% relative humidity. The separators were then dried at 70 °C for 12 h using a temperaturecontrolled vacuum oven to completely remove all traces of moisture. The thickness of the coated separator was measured by a micrometer (Mitutoyo, Japan) with an accuracy of 1 µm. The final thickness was found to be 40 μm . About 10 μm compression was observed due to drying of the separator.

For measuring the pore structure of the zeolite separators, the coated separator on the aluminum foil peeled off carefully without causing any physical damage to the separator. This free-standing zeolite separator was obtained to match the physical free-standing nature of the PP-2500 separator. The porosity (\emptyset) of the separator was obtained from the measured bulk density (using the weight and dimensional volume of the coated zeolite separator) using Eq. (1) [35]:

$$\emptyset = 1 - \frac{\rho_{bulk}}{\rho_{particle}} \tag{1}$$

To measure the tortuosity of the PP-2500 and zeolite separators, a

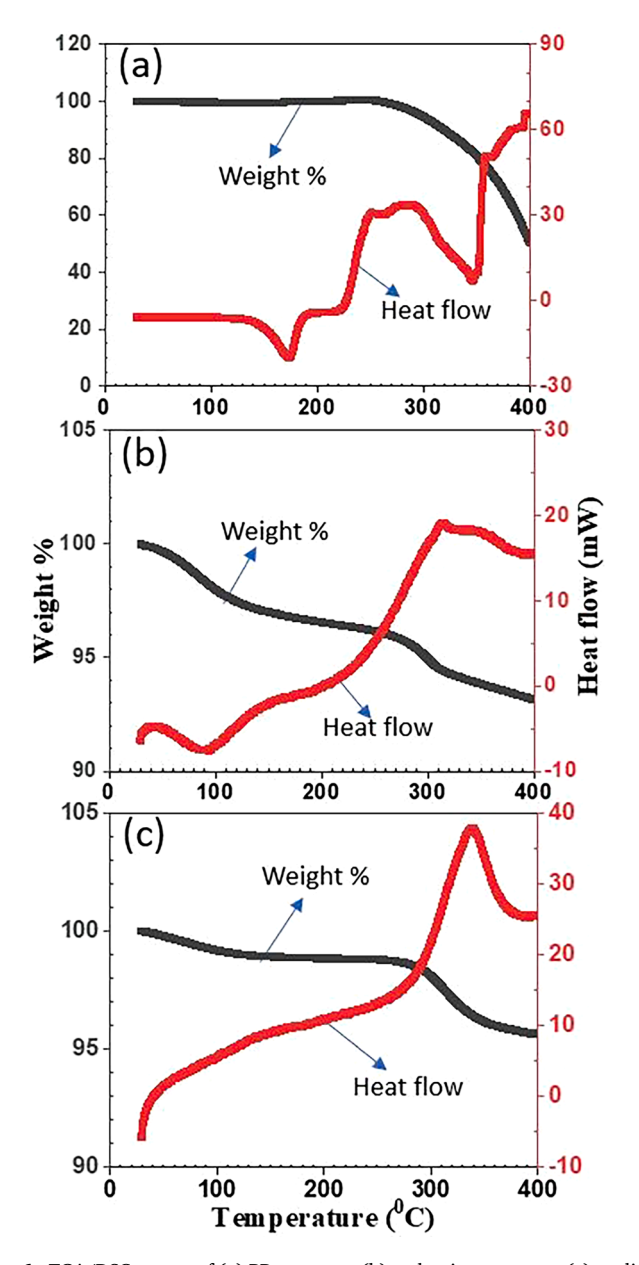
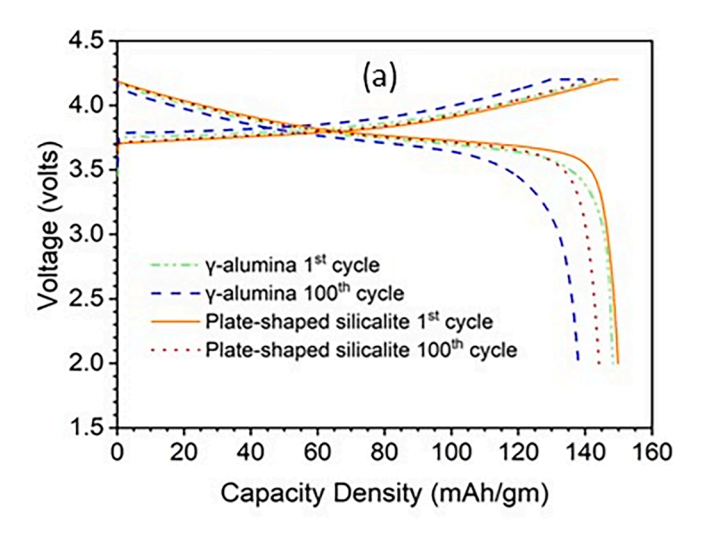


Fig. 6. TGA/DSC curves of (a) PP separator (b) γ -alumina separator (c) zeolite (silicalite) separator.

free-standing zeolite separator was soaked in electrolyte for 24 h inside the glovebox. After this step, the soaked separator was inserted between two stainless steel electrode plates, which had the same shape and cross-section as the free-standing separator. The ohmic resistance of the separator was then obtained by using electrochemical impedance spectroscopy (PARSTAT 2263 EIS station, Princeton Applied Research, USA) at 25 °C. EIS instrument scanning parameters were set to a starting frequency of 100 kHz and ending frequency of 100 mHz, with an AC amplitude of 10 mV rms. The tortuosity (τ) of the electrolyte-filled separator is related to its measured ohmic resistance (R) and the intrinsic conductivity of the electrolyte (σ) by the following equation [36]:

$$\tau = \frac{\sigma \times \emptyset}{\sigma_{ven}} \tag{2}$$

with



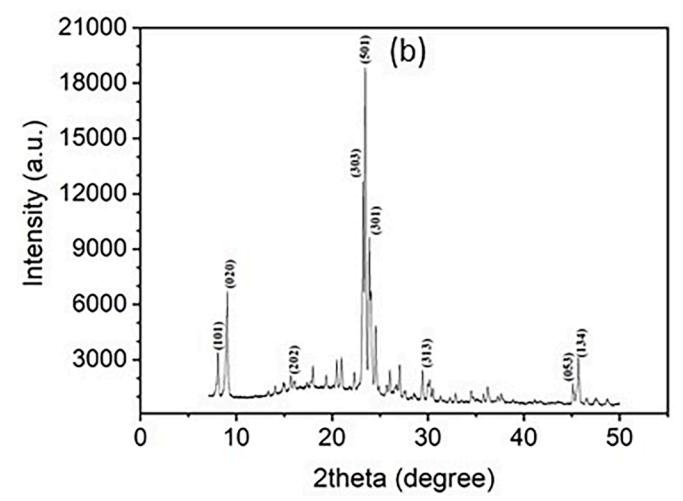


Fig. 7. (a) Voltage versus capacity density curves for the 1st and 100th cycle for γ -alumina and plate-shaped zeolite (silicalite) separators when cycled at a 0.2 C-rate; and (b) XRD pattern for the extracted cycled electrode coated with plate-shaped zeolite separator post 100 cycles at a 3C-rate.

$$\sigma_{sep} = \frac{d}{AR} \tag{3}$$

where σ_{sep} is conductivity for the electrolyte-filled separator, \emptyset is the porosity of the separator, d is the thickness of the separator, and A is the cross-sectional area of the separator.

The crystal structure of the zeolite powders and coated separators was examined by X-ray diffraction (Bruker AXS-D8, Cu Kα radiation, USA). The surface and cross-sectional morphology of the coated zeolite separators, after being sputter-coated with gold, was examined by scanning electronic microscopy (SEM) (Philips, USA, FEI XL-30). Topview SEM images of the zeolite separators on aluminum foil were quantified for particle size distribution using GATAN GMS software with the particle size interval being 0.25 µm. The zeolite-coated aluminum foils were cut into 16 mm disks and tested for their pore size distribution using a mercury porosimeter (Micrometrics Auto Pore V, USA). Contact angle of the 1 M LiPF₆ in 1:1:1 (v/v/v) ethyl carbonate/dimethyl carbonate/diethyl carbonate electrolyte on the zeolite and alumina separator films on aluminum foil and PP separator was measured by a Kruss Easy drop goniometer. For TGA/DSC analysis, the zeolite and alumina separator films peeled off from the aluminum foil and PP separator were broken into small pieces to fit them into the crucible on a TGA/DSC equipment (Labsys Evo from Setaram). The samples were heated from 20 °C to 400 °C at the ramping rate of 10 °C/min in the atmosphere of

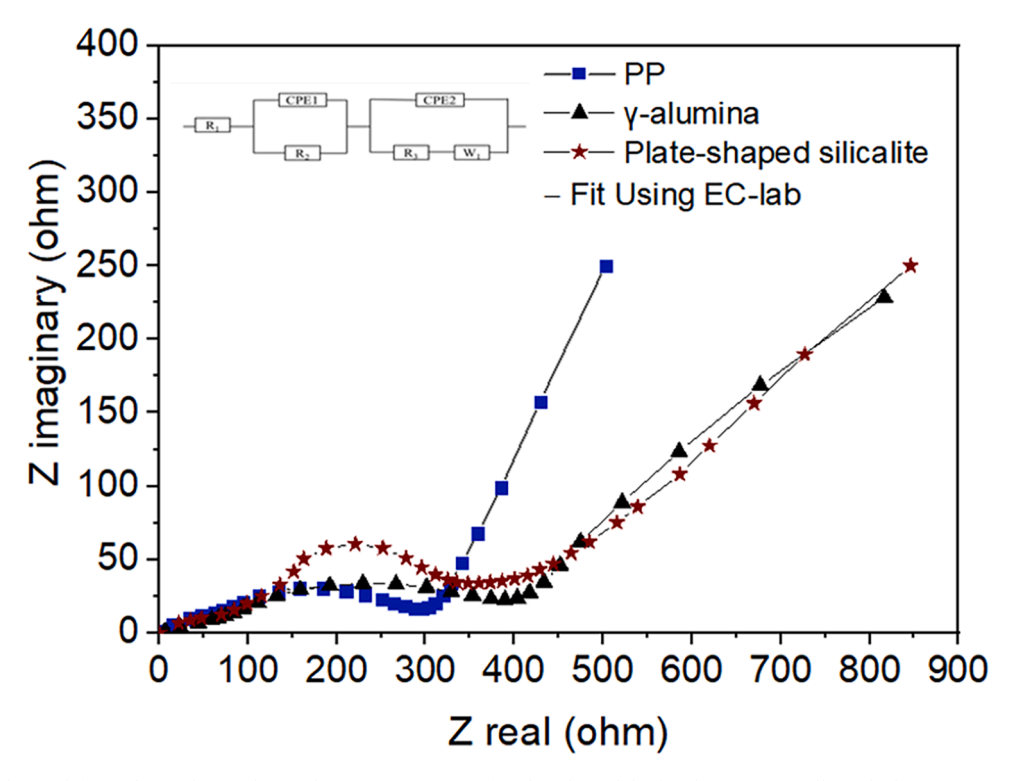


Fig. 8. Nyquist plot obtained from electrochemical impedance spectroscopy (fitted with EC-lab) for the NCM/Li cells with the separator of plate-shaped zeolite (silicalite), γ-alumina and polypropylene (PP).

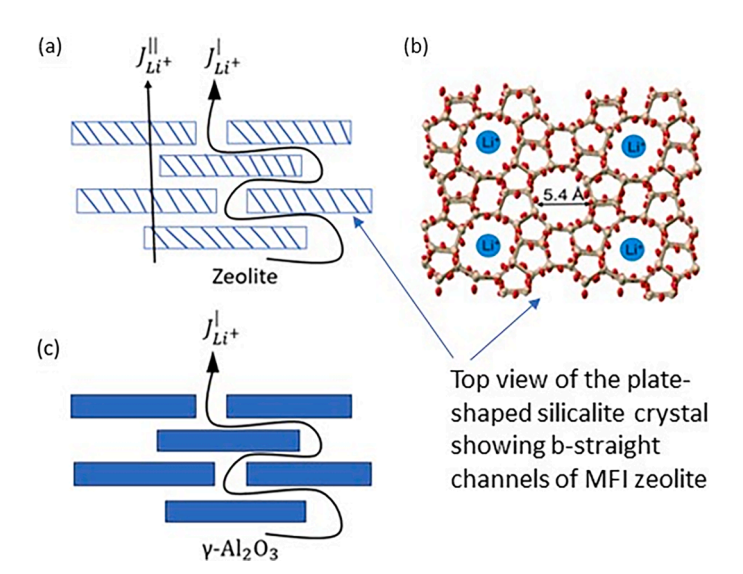


Fig. 9. (a) Schematic illustration of two pathways for lithium-ion flux through electrolyte-filled separator made of plate-shaped MFI zeolite with (b) top view of b-axis crystalline pore structure of MFI zeolite and (c) schematic illustration of one pathway for lithium-ion flux through electrolyte-filled separator made of dense plate-shaped γ -alumina particles.

ultra-pure air.

2.3. Coin-cell construction and analysis of post-cycling cell internals

Zeolite separator-coated NMC electrode disks of 16 mm diameter were cut from the corresponding coated electrode sheets and then kept in a vacuum oven at 70 $^{\circ}$ C for 12 h. They were then immediately placed in an argon-filled glovebox (Innovative Technology Inc., USA) for a period of 24 h to remove any traces of atmospheric gasses or moisture in

the electrode-supported separator disks. The other components of the cell were already kept for assembly in the glovebox. The 16 mm electrode-supported separator disk was placed inside the bottom case of the CR-2032 cell, with the separator facing up, and 150 μl of electrolyte (1 M LiPF $_6$ salt in equal volumes of EC:DEC:DMC) was pipetted onto the surface of the zeolite coated NMC electrode. A lithium metal chip was then very carefully placed on top of the separator surface. Two spacers and one spring (X2 Labwares, Singapore) were then placed on the lithium anode, followed by the placement of the top case of the CR-2032 cell to closely envelop the full cell. The coin cell was then crimped to a pressure of 400 psi. The zeolite separator coated on NMC post 400 psi compression was also examined by XRD to see if there was any change in the crystal orientation.

The assembled lithium-metal coin cell filled with the electrolyte was then taken out, and its charge and discharge characteristics were tested by a battery testing system (Neware Co., China). The cells with zeolite separator were tested at various C-rates (from 0.2 C to 3 C-rate) between 2.0 to 4.2 Vs for 100 cycles, with the standard CC—CV (constant current—constant voltage) method. PARSTAT 2263 EIS station (Princeton Applied Research, USA) was used in the AC mode to perform electrochemical impedance spectroscopy (EIS) measurements of the assembled cells. Nyquist plots for the assembled half cells were generated by utilizing a frequency range of 100 kHz to 100 mHz.

To examine the stability and propagation of dendrites through the separator, the zeolite separators were extracted from NMC/zeolite-separator/Li coin-cells post-cycling at a 3 C-rate for 100 cycles. The cycled coin cells with the zeolite separator were disassembled inside the glovebox. The lithium metal anode was removed from the cell, and the zeolite separator-coated NMC cathode was placed on an SEM sample holder stage. This sample holder was then taken for gold sputtering inside a vacuum-sealed container, and the surface of the separator in contact with the lithium metal anode was then examined for the presence of Li dendrites. The use of this SEM technique for the investigation of battery materials has been established in the literature [37].

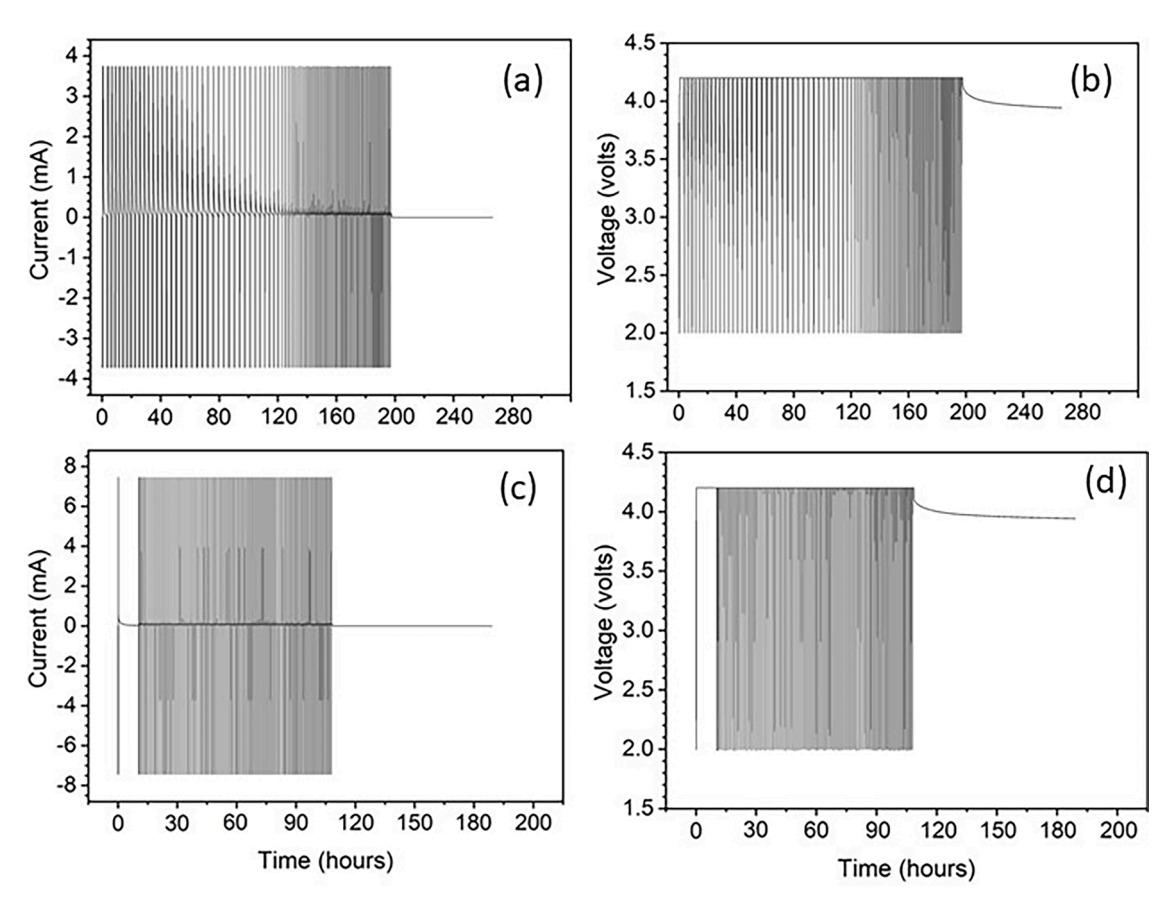


Fig. 10. Charge and discharge profiles for the lithium metal cell with plate-shaped zeolite (silicalite) separator at a 1 C-rate (a) current vs. time and (b) voltage vs. time; and at 2 C-rate (c) current vs. time and (d) voltage vs. time.

3. Results and discussion

3.1. Characteristics of zeolite powder and coated separators

Fig. 1(a) shows the SEM micrograph of the synthesized plate-shaped zeolite particles when they were formed as a coated separator on the NMC electrode. These particles have also been described as coffinshaped particles [38], and have an edge thickness of 0.1-0.2 nm, a width of 2–4 μm, and a length of 2–6 μm. The aspect ratio is defined as the ratio of the length to the thickness, which is about 20-60 for the plate-shaped zeolite. We can also observe that some of the larger particles have broken down due to the wet grinding process, which results in several rectangular plate-shaped particles. Fig. 1(b) shows the average particle size distribution of the SEM image from Fig. 1(a), plotted as a function of particle number density. The number-based size distribution skews toward the smaller particles. The majority of the particles are in the 2.0 to 2.5 µm range, which is similar to the range in which the NMC electrode pore sizes are observed as well [32]. The particle size range of the plate-shaped zeolite particles was designed to match the pore size of the NMC electrode to achieve a high-quality coating of separator in a single coat, as has been seen reported in our previous work [32,39]. The morphology and particle size distribution of γ -alumina particles prepared in our lab [31] are presented in Fig. 1(c) and (d) for comparison. These γ -alumina particles are also of plate shape with average particle size similar to the plate-shaped zeolite. However, γ -alumina particles are dense without intraparticle pores.

Fig. 2 shows the XRD pattern of the synthesized zeolite powder, the zeolite membrane coated on the NMC cathode before compression, and the zeolite membrane on the NMC cathode after compression. Major peaks marked with the miller indices are representative of those for MFI type zeolite noted in the literature [40,41]. Diffraction peaks for the

powder sample (Fig. 2(a)) are characteristic of the powder XRD pattern of MFI zeolite. The XRD patterns for the zeolite membrane separator coated on the cathode before compression (Fig. 2(b)) and after compression at 400 psi (Fig. 2(b)) show the same diffraction peaks as the powder sample. No peaks from the NMC and aluminum foil are seen in the two diffraction patterns of zeolite separators coated on the NMC cathode because of the large thickness of the coated zeolite layer. Compared to the powder sample, the two membrane samples show enhancement in the XRD peak intensity for the (020) plane. The ratio of the peak intensity for the (020) plane to that of the (101) plane increases from 0.8 for the powder sample (Fig. 2(a)), to 0.9 for coated zeolite membrane before compression (Fig. 2(b)), and 2.5 for the coated zeolite membrane after compression at 400 psi (Fig. 2(c)). It is known that plate-shaped MFI zeolite crystals have large flat surface (010) normal to b-axis straight channels for MFI zeolite, as shown in Fig. 3(a) [42,43]. This suggests that coating or coating followed by compression has caused the orientation of the plate-shaped zeolite particles along the flat plane of the zeolite crystals. The compression, with force acting in a direction normal to the cathode surface, helped orient the plate-shaped silicalite particles with large planes to align parallel to the surface of the NMC electrode, as shown in Fig. 3(b). Thus, the b-axis straight intracrystalline pores are better aligned with the lithium-ion flux direction during the operation of lithium-metal battery cells.

Fig. 4(a) shows the cross-sectional SEM image of the plate-shaped zeolite separator coated on the NMC electrode on aluminum foil. We can see that the separator is evenly coated over the NMC electrode with a thickness of $\sim 40~\mu m$. It should be noted that the minimum thickness for the zeolite separator coated on a cathode depends on a number of factors, including the smoothness and pore structure of the cathode surface. With the NCM from MTI used in this work, it was difficult to obtain a good performing zeolite separator with a thickness below 30–40 μm . The

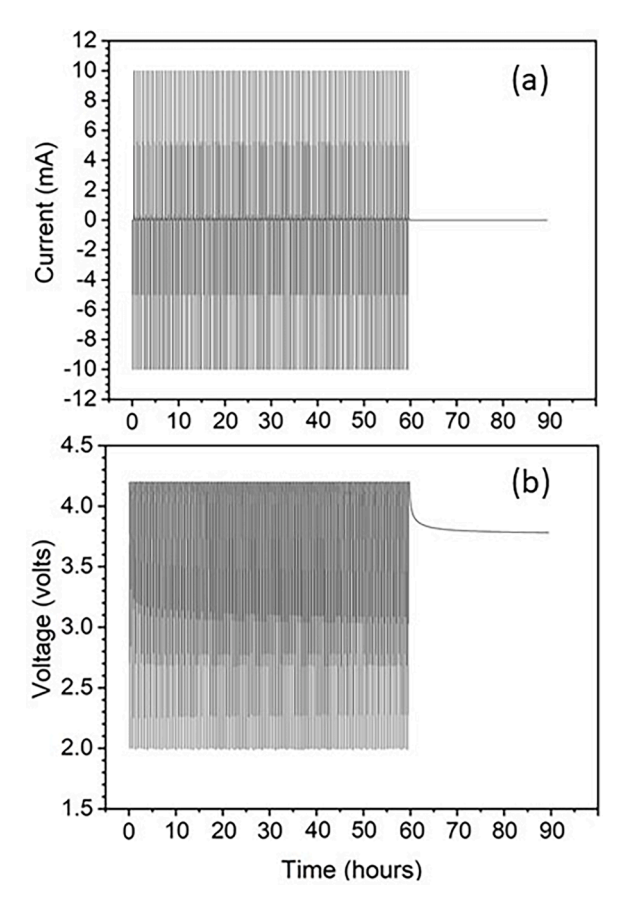


Fig. 11. Charge and discharge profiles for the lithium metal cell with plate-shaped zeolite (silicalite) separator at 3 C-rate (a) current vs. time; and (b) voltage vs. time for 100 cycles.

EIS study shows ohmic resistance for a 40 um zeolite separator, similar to a 25 um PP separator, is significantly smaller than the charge transfer resistance, suggesting that a 40 um thick zeolite separator has a limited effort on cell performance. Fig. 4(b) shows the pore size distribution of the plate-shaped zeolite and the γ -alumina separators when coated on aluminum foil, as obtained via mercury porosimetry. The intraparticle micropores (pore diameter about 0.6 nm) in the plate-shaped zeolite particles cannot be observed as the mercury porosimeter is unable to detect them due to instrument limitation. Table 1 lists the pore structure and tortuosity of the zeolite separator measured in this work and for the γ -alumina separator reported previously [31]. We can see that the pore size of the plate-shaped zeolite separator (~ 450 nm) is remarkably similar to the γ -alumina separator (~430 nm). As discussed in the introduction, the γ-alumina separator was examined in our previous study [31] to determine the effect of separator pore tortuosity on dendrite propagation. In the present study, we designed the separator particles to have a pore size similar to the γ -alumina separator, so that the effect of the zeolite intra-particle pores on Li-ion transport could be evaluated.

Fig. 5 shows the results of contact angle tests for the 1 M LiPF6 in 1:1:1 (v/v/v) ethyl carbonate/dimethyl carbonate/diethyl carbonate electrolyte on zeolite, alumina, and PP separators. The contact angle for the liquid electrolyte at 1 s on the PP separator is 51.06° , while that for the zeolite and alumina separators is zero. From the above results, it can be inferred that the alumina and zeolite separators are highly wettable for the liquid electrolyte as compared to the organic PP separator. Fig. 6 gives the results of the TGA/DSC analysis of the three separators in the air. The TGA data show approximately 52%, 7%, and 5% loss of mass observed with the PP separator, alumina separator, and zeolite separator, respectively from room temperature to 400 °C. The PP separator

incurred much greater mass loss compared to the other separators. Two endotherm peaks are observed with the PP separator. The first peak between 160 °C and 180 °C corresponds to the melting temperature, and the second peak between 340 °C and 360 °C is related to the degradation of the material (combustion). The endothermic peak and mass loss observed with the γ -alumina separator at 100 °C are due to the loss of the trace amount of water present in the sample. The exothermic peak seen at 310 °C corresponds to the oxidative decomposition of the PVA present in the separator. It decomposes rapidly above 200 °C. Similarly, the mass loss and the exothermic peak observed with the zeolite (silicalite) separator infers the loss of traces of water and decomposition of PVA. The zeolite and alumina separators are thermally very stable, as expected from their composition of pure SiO2 and Al2O3.

3.2. Electrochemical characterization, coin-cell performance, and separator evaluation

Fig. 7(a) shows the 1st and 100th V-C curves for the NMC/Li-metal cells with plate-shaped zeolite and γ -alumina separators cycled at a 0.2 C-rate. The cell with a zeolite separator has a flatter discharge profile compared to the γ -alumina separator in the lithium metal cell. Also, the cell with the zeolite separator lost about 4% less capacity at the end of 100 cycles compared to the γ -alumina separator. Overall, the cell with the zeolite separator performed better than the cell with the γ -alumina separator. Fig. 7(b) shows the XRD pattern of the cycled zeolite separator post 100 cycles at a 3 C-rate. The peaks are similar to those obtained post compression, as seen in Fig. 2(c). Thus, the separator is stable during and post cycling. The peak intensities vary slightly between the two figures; however, the peak locations remain the same, confirming that there is no structural change in the separator.

Fig. 8 shows the Nyquist plots obtained from EIS measurements for the coin cells with zeolite, γ -alumina and PP separators. The quantified values of the ohmic, SEI, and charge-transfer resistances obtained from the EIS data using EC-lab software are listed in Table 1. We observe that the ohmic, SEI and charge-transfer resistances for the cell with PP separator are smaller than those for the cells with zeolite and γ -alumina separators due in part to the smaller thickness and low tortunity for the PP separator. The ohmic resistance of the zeolite separator is about 2% larger than that of γ -alumina, but the SEI layer and charge transfer resistances for the cell with zeolite separator is about 10% smaller than the cell with γ -alumina separator. The better charge/discharge performance of the cell with the zeolite separator is clearly due to its lower SEI and charge transfer resistance as compared to the cell with the γ -alumina separator.

The difference in electrochemical characteristics and charge/ discharge performance between the cells with the zeolite and γ-alumina separator can be discussed qualitatively in terms of differences in their morphology and microstructure shown in Fig. 1. As mentioned before, the zeolite plates have a thickness of 0.1–0.2 µm, a width of 2–4µm, and a length of 2-6 µm with an average aspect ratio of about 40. The γ -alumina particles are also plate-shaped. However, from Fig. 1, the γ -alumina plates are slightly thicker and smaller than zeolite plates. The average sizes of γ -alumina plates are $\sim 0.5 \times 3 \times 3 \mu m$, giving an aspect ratio of ~6, smaller than that for the plate-shaped zeolite. The pore tortuosity of the plate-packed membranes increases with the aspect ratio of the plates. Thus, one should expect larger tortuosity for the zeolite separator than the γ -alumina separator. However, our measured tortuosity for the zeolite separator is even slightly smaller than the γ -alumina separator (Table 1). It is important to note that zeolite plates contain crystalline intraparticle pores (zeolitic pores), while γ -alumina plates are dense particles without intraparticle pores.

For a separator with a given pore structure, Eq. (2) shows that smaller tortuosity measured for the zeolite separator means a larger ionic conductivity for the electrolyte-filled zeolite separator. Since both zeolite and γ -alumina separators have the same interparticle porosity, the larger conductivity for the electrolyte-filled zeolite separator

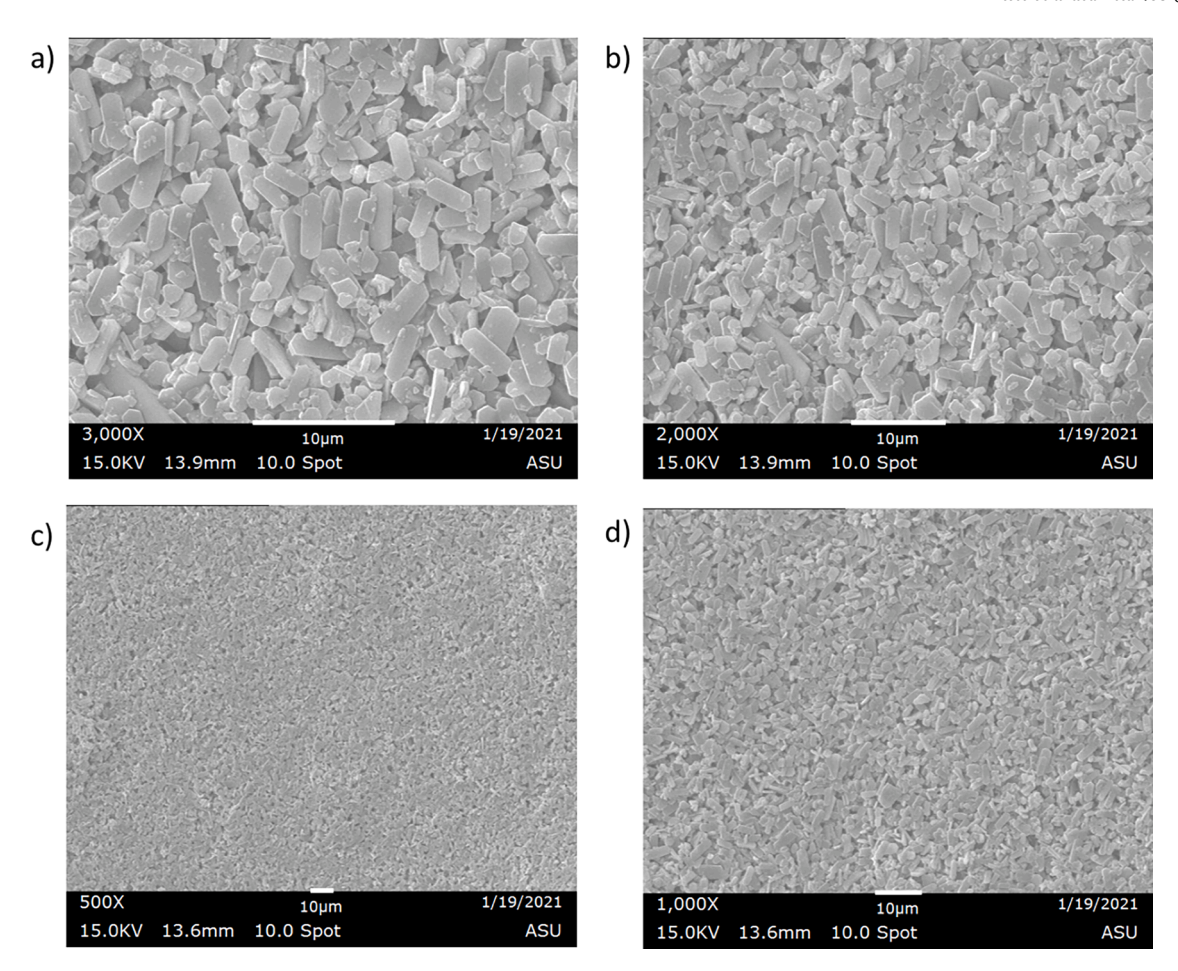


Fig. 12. The top-view SEM micrographs at various magnifications (a-d) of the extracted plate-shaped zeolite (silicalite) separator surface post 100 cycles at 3 C-rate.

indicates considerable Li-ion flux through the interparticle pores of zeolite plates. The oriented packing of MFI zeolite with straight bchannels normal to the cathode surface, as shown in Figs. 3(b) and 9(a). could further facilitate the transport of Li-ion within intraparticle pores (Fig. 9(b)). Thus, for the cell with the zeolite separator, Li-ions transport through both interparticle (pathway I) and intraparticle (pathway II) pathways, as illustrated in Fig. 9(a). Though Li-ions transport primarily through the intercrystalline pores due to their large pore size and high porosity shown in Table 1, the transport of Li-ions through intracrystalline pores results in a more uniform Li-ion flux at the separatoranode interface, which is known to result in a more uniform and robust solid-electrolyte interface (SEI) and better availability of the Liions at the lithium metal anode, leading to significantly enhanced performance of lithium-metal battery cells [44,45]. The Li-ion transference number for LiPF₆ in carbonate solvent is in 0.3–0.4 [46]. For the zeolite separator, the bulkier PF₆ anion can be difficult to enter the MFI zeolite intracrystalline pores (0.55 nm). Furthermore, at the steady state, diffusion flux and migration flux for PF⁶⁻ are the same, so there is no net transport of PF₆. Thus, in discussing ion transport through intracrystalline pores, one only needs to consider the transport of Li-ions. For a separator made of dense plate-shaped γ -alumina particles, Li-ions can transport through an interparticle pathway, as shown in Fig. 9(c), providing less uniform Li-ion flux at the separator-anode interface. This explains the better performance of the cell with the zeolite separator than that with the γ -alumina separator.

Charge and discharge current and voltage profiles versus time when the LMB cell with the zeolite separator was cycled at 1 C-rate and 2 C-rate are shown in Fig. 10. As we can clearly see from Fig. 10(a) and (c), the cell reaches its full rated charge and discharge current while cycling at a 1 C-rate and 2 C-rate. This implies that there is no substantial active

lithium metal lost during the cycling from the anode, which otherwise would reduce the overall capacity of the battery. If substantial active material was being lost into the separator in the form of dendrites or lost as non-reactive lithium metal defects, the battery would not have been able to reach this charge/discharge rate [47,48]. From Fig. 10(b) and (d), we can observe that the voltage profiles for these batteries are stable during the entire 100 cycles. This indicates that no dendrites have propagated through the separator, Otherwise, the cell would have shown a sudden drop in voltage even at a maximum rate of charging. These voltage and current profiles suggest that this separator with higher pore tortuosity, similar to the γ -alumina separator, prevents the formation and propagation of dendrites at these charge/discharge rates.

Fig. 11 presents the voltage and current trends versus time for the LMB cell with the zeolite separator while charging and discharging at a 3 C-rate. The current during charge and discharge for the plate-shaped zeolite separator reaches its full range for the complete 100 cycles, whereas the cell with the γ -alumina separator starts losing its capacity at around the 75th cycle [31]. Thus, we can see that the presence of the intraparticle pores of the zeolite particles facilitates better Li-ion distribution across the separator and anode interface. This enables more uniform plating of lithium on the metal anode at high C-rates, reducing the amount of inactive lithium which would have dislodged from the lithium metal anode and deposited into the separator. Furthermore, the voltage profile is also stable for the entire range of 100 cycles, confirming that no dendrites have propagated through the separator. Also, the cell voltage remains constant at around 3.8 Vs post-cycling, which is an indication of a stable cell.

Fig. 12 (a–d) show the top-view SEM images of the surface of the zeolite separator on the NMC cathode extracted from an LMB cell post-cycling at a 3 C-rate for 100 cycles. There are no visible foreign materials

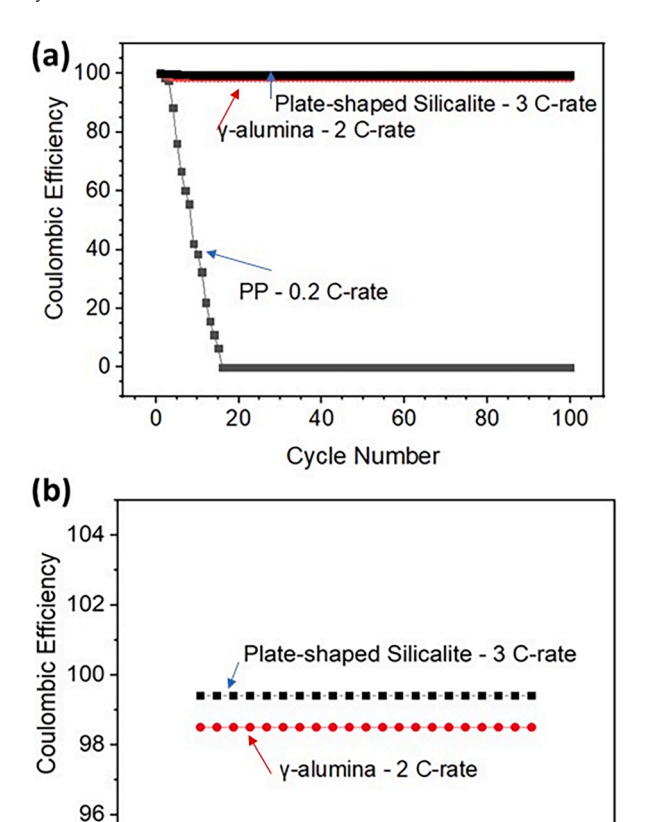


Fig. 13. (a) Columbic efficiency of LMB cells with plate-shaped zeolite (silicalite) separator (at 3 C-rate), γ -alumina (at 2 C-rate), and polypropylene (PP) separator (at 0.2 C-rate); and (b) enlarged view of the Columbic efficiency for LMB cells with plate-shaped zeolite (silicalite) separator (at 3 C-rate) and γ -alumina (at 2 C-rate).

90

Cycle Number

95

85

100

105

on the zeolite particles or within the visible pores of the zeolite separator. This confirms that the separator has no dislodged lithium metal or lithium metal dendrite remnants within the separator matrix. This result is consistent with the stable voltage and current versus time profiles, as observed in Fig. 10(a) and (b).

Fig. 13 compares the Columbic efficiency for the LMB cells with separators made of plate-shaped zeolite and γ -alumina. As shown, both cells have essentially 100% Columbic efficiency, at least for up to 100 cycles. The enlarged view in Fig. 13(b) shows that the cell with the zeolite separator at a 3 C-rate performs better than that with the γ -alumina separator at a 2 C-rate. For comparison, the Columbic efficiency for the LMB cell with a conventional polypropylene (PP, Celgard 2500) separator stops functioning after about 15 cycles, even at a much lower C-rate, as shown in Fig. 13(a). These results further confirm the advantages of using plate-shaped zeolite with intraparticle micropores as a separator for stable lithium-metal batteries.

4. Conclusions

75

80

Plate-shaped zeolite particles can be synthesized in-house using a modified hydrothermal method to produce particles of a specific particle-size range. These zeolite particles were formed into a slurry, which can be coated on cathode by a blade-coating method to form tortuous electrode-coated separators of required thickness. The zeolite separators have lower SEI and charge transfer resistance as compared to a similar tortuously porous separator made of dense plate-shaped γ -alumina particles. While cycling at a 3 C-rate, the lithium-metal

battery (LMB) cell with the γ -alumina separator started to lose capacity by the 75th cycle, while the cell with the zeolite separator did not lose any capacity for the entire 100 cycles. Thus, LMB cells with a plate-shaped zeolite separator having intraparticle pores perform better than the cells with a separator without these pores (γ -alumina). For lithium-metal batteries with plate-shaped zeolite separators, the highly tortuous pores of the zeolite separator inhibit dendrite growth/propagation, and the intraparticle pores of the zeolite assist in homogenizing the Li-ion flux at the separator-anode interface. This leads to stable cycling of the lithium-metal battery with zeolite separator even at high C-rates without any dendrite propagation. This electrode-coated plate-shaped zeolite separator provides a commercially viable route for the development of safe and long-lasting lithium-metal batteries.

CRediT authorship contribution statement

Kishen Rafiz: Investigation, Formal analysis, Data curation, Methodology, Writing – original draft. **N.R.D. Harika:** Investigation, Formal analysis, Data curation, Writing – original draft. **Jerry Y.S. Lin:** Methodology, Formal analysis, Resources, Supervision, Project administration, Funding acquisition, Writing – review & editing.

Declaration of Competing Interest

The authors declare the following financial interests/personal relationships which may be considered as potential competing interests: Arizona State University has entered into license agreements with Safe-Li LLC and Safe-LiMax LLC on development of zeolite membrane separator technology for safe-lithium-ion batteries and lithium-metal batteries. JYSL is a co-founder and Chief Science Officer of these two startups.

Data availability

Data will be made available on request.

Acknowledgement

We acknowledge the support of the National Science Foundation (CBET-2031087, CBET-2200204) on zeolite membrane research from which this project benefits and the ASU Catalysis Fund for supporting the work.

References

- [1] Y. An, Z. Zhang, H. Fei, X. Xu, S. Xiong, J. Feng, L. Ci, Lithium metal protection enabled by in-situ olefin polymerization for high-performance secondary lithium sulfur batteries, J. Power Sources 363 (2017) 193–198, https://doi.org/10.1016/j. jpowsour.2017.07.101.
- [2] B. Dunn, H. Kamath, J.M. Tarascon, Electrical energy storage for the grid: a battery of choices, Science 334 (2011) 928–935, https://doi.org/10.1126/ science.1212741.
- [3] W. Xu, J. Wang, F. Ding, X. Chen, E. Nasybulin, Y. Zhang, J.G. Zhang, Lithium metal anodes for rechargeable batteries, Energy Environ. Sci. 7 (2014) 513–537, https://doi.org/10.1039/C3EE40795K.
- [4] N.W. Li, Y.X. Yin, C.P. Yang, Y.G. Guo, An artificial solid electrolyte interphase layer for stable lithium metal anodes, Adv. Mater. 28 (2016) 1853–1858, https://doi.org/10.1002/adma.201504526
- [5] D. Aurbach, E. Zinigrad, Y. Cohen, H. Teller, A short review of failure mechanisms of lithium metal and lithiated graphite anodes in liquid electrolyte solutions, Solid State Ionics 148 (2002) 405–416, https://doi.org/10.1016/S0167-2738(02)00080-2
- [6] K.J. Harry, D.T. Hallinan, D.Y. Parkinson, A.A. MacDowell, N.P. Balsara, Detection of subsurface structures underneath dendrites formed on cycled lithium metal electrodes. Nat. Mater. 13 (2014) 69–73. https://doi.org/10.1038/nmat3793.
- [7] G. Zheng, S.W. Lee, Z. Liang, H.W. Lee, K. Yan, H. Yao, H. Wang, W. Li, S. Chu, Y. Cui, Interconnected hollow carbon nanospheres for stable lithium metal anodes, Nat. Nanotechnol. 9 (2014) 618–623, https://doi.org/10.1038/nnano.2014.152.
- [8] J.W. Fergus, Ceramic and polymeric solid electrolytes for lithium-ion batteries, J. Power Sources 195 (2010) 4554–4569, https://doi.org/10.1016/j. jpowsour.2010.01.076.

- [9] C. Brissot, M. Rosso, J.N. Chazalviel, P. Baudry, S. Lascaud, *In situ* study of dendritic growth inlithium/PEO-salt/lithium cells, Electrochim. Acta 43 (1998) 1569–1574, https://doi.org/10.1016/S0013-4686(97)10055-X.
- [10] W. Liu, W. Li, D. Zhuo, G. Zheng, Z. Lu, K. Liu, Y. Cui, Core-shell nanoparticle coating as an interfacial layer for dendrite-free lithium metal anodes, ACS Cent. Sci. 3 (2017) 135–140, https://doi.org/10.1021/acscentsci.6b00389.
- [11] P.J.H. Kim, V.G. Pol, Surface functionalization of a conventional polypropylene separator with an aluminum nitride layer toward ultrastable and high-rate lithium metal anodes, ACS Appl. Mater. Interfaces 11 (2019) 3917–3924, https://doi.org/ 10.1021/acsami.8b18660.
- [12] M. Kim, G.Y. Han, K.J. Yoon, J.H. Park, Preparation of a trilayer separator and its application to lithium-ion batteries, J. Power Sources 195 (2010) 8302–8305, https://doi.org/10.1016/j.jpowsour.2010.07.016.
- [13] X.B. Cheng, R. Zhang, C.Z. Zhao, Q. Zhang, Toward safe lithium metal anode in rechargeable batteries: a review, Chem. Rev. 117 (2017) 10403–10473, https://doi.org/10.1021/acs.chemrev.7b00115.
- [14] C. Monroe, J. Newman, The impact of elastic deformation on deposition kinetics at lithium/polymer interfaces, J. Electrochem. Soc. 152 (2005) A396, https://doi. org/10.1149/1.1850854
- [15] W.K. Shin, D.W. Kim, High performance ceramic-coated separators prepared with lithium ion-containing SiO2 particles for lithium-ion batteries, J. Power Sources 226 (2013) 54–60, https://doi.org/10.1016/j.jpowsour.2012.10.082.
- [16] H. Xiang, J. Chen, Z. Li, H. Wang, An inorganic membrane as a separator for lithium-ion battery, J. Power Sources 196 (2011) 8651–8655, https://doi.org/ 10.1016/j.ipowsour.2011.06.055.
- [17] H. Shen, E. Yi, L. Cheng, M. Amores, G. Chen, S.W. Sofie, M.M. Doeff, Solid-state electrolyte considerations for electric vehicle batteries, Sustain. Energy Fuels 3 (2019) 1647–1659, https://doi.org/10.1039/C9SE00119K.
- [18] A. Gurung, J. Pokharel, A. Baniya, R. Pathak, K. Chen, B. Sagar Lamsal, N. Ghimire, W.H. Zhang, Y. Zhou, Q. Qiao, A review on strategies addressing interface incompatibilities in inorganic all-solid-state lithium batteries, Sustain. Energy Fuels 3 (2019) 3279–3309, https://doi.org/10.1039/C9SE00549H.
- [19] E. Rangasamy, Z. Liu, M. Gobet, K. Pilar, G. Sahu, W. Zhou, H. Wu, S. Greenbaum, C. Liang, An iodide-based Li7P2S8I superionic conductor, J. Am. Chem. Soc. 137 (2015) 1384–1387, https://doi.org/10.1021/ja508723m.
- [20] S. Wenzel, T. Leichtweiss, D. Krüger, J. Sann, J. Janek, Interphase formation on lithium solid electrolytes—an in situ approach to study interfacial reactions by photoelectron spectroscopy, Solid State Ion. 278 (2015) 98–105, https://doi.org/ 10.1016/j.ssi.2015.06.001.
- [21] P. Bai, J. Guo, M. Wang, A. Kushima, L. Su, J. Li, F.R. Brushett, M.Z. Bazant, Interactions between lithium growths and nanoporous ceramic separators, Joule 2 (2018) 2434–2449. https://doi.org/10.1016/j.joule.2018.08.018.
- [22] W. Qu, M. Yan, R. Luo, J. Qian, Z. Wen, N. Chen, L. Li, F. Wu, R. Chen, A novel nanocomposite electrolyte with ultrastable interface boosts long life solid-state lithium metal batteries, J. Power Sources 484 (2021), 229195, https://doi.org/ 10.1016/j.jpowsour.2020.229195.
- [23] H.M.J.C. Pitawala, M.A.K.L. Dissanayake, V.A. Seneviratne, Combined effect of Al2O3 nano-fillers and EC plasticizer on ionic conductivity enhancement in the solid polymer electrolyte (PEO)9LiTf, Solid State Ion. 178 (2007) 885–888, https://doi.org/10.1016/j.ssi.2007.04.008.
- [24] S. Ito, A. Unemoto, H. Ogawa, T. Tomai, I. Honma, Application of quasi-solid-state silica nanoparticles-ionic liquid composite electrolytes to all-solid-state lithium secondary battery, J. Power Sources 208 (2012) 271–275, https://doi.org/ 10.1016/j.joowsour.2012.02.049.
- [25] K. Liu, A. Pei, H.R. Lee, B. Kong, N. Liu, D. Lin, Y. Liu, C. Liu, P. Hsu, Z. Bao, Y. Cui, Lithium metal anodes with an adaptive "solid-liquid" interfacial protective layer, J. Am. Chem. Soc. 139 (2017) 4815–4820, https://doi.org/10.1021/jacs.6b13314.
 [26] J. Liang, Q. Chen, X. Liao, P. Yao, B. Zhu, G. Lv, X. Wang, X. Chen, J. Zhu, A nano-
- [26] J. Liang, Q. Chen, X. Liao, P. Yao, B. Zhu, G. Lv, X. Wang, X. Chen, J. Zhu, A nano-shield design for separators to resist dendrite formation in lithium-metal batteries, Angew. Chem. Int. Ed. 59 (2020) 6561–6566, https://doi.org/10.1002/anie.201915440.
- [27] N. Li, W. Wei, K. Xie, J. Tan, L. Zhang, X. Luo, K. Yuan, Q. Song, H. Li, C. Shen, E. M. Ryan, L. Liu, B. Wei, Suppressing dendritic lithium formation using porous media in lithium metal-based batteries, Nano Lett. 18 (2018) 2067–2073, https://doi.org/10.1021/acs.nanolett.8b00183.
- [28] Z. Rao, Z. Yang, W. Gong, S. Su, Q. Fu, Y. Huang, Simultaneously suppressing lithium dendrite growth and Mn dissolution by integration of a safe inorganic separator in a LiMn 2 O 4 /Li battery, J. Mater. Chem. A 8 (2020) 3859–3864, https://doi.org/10.1039/C9TA12979K.

- [29] M.B. Dixit, M. Regala, F. Shen, X. Xiao, K.B. Hatzell, Tortuosity effects in garnettype Li7La3Zr2O12 solid electrolytes, ACS Appl. Mater. Interfaces 11 (2019) 2022–2030, https://doi.org/10.1021/acsami.8b16536.
- [30] A. Hussain, D. Li, Y. Luo, H. Zhang, H. Zhang, X. Li, Porous membrane with improved dendrite resistance for high-performance lithium metal-based battery, J. Memb. Sci. 605 (2020), 118108, https://doi.org/10.1016/j. perperi 2020 118108
- [31] K. Rafiz, D.R.L. Murali, J.Y.S. Lin, Suppressing lithium dendrite growth on lithiumion/metal batteries by a tortuously porous γ-alumina separator, Electrochim. Acta 421 (2022), https://doi.org/10.1016/j.electacta.2022.140478.
- [32] K. Rafiz, J.Y.S. Lin, Safe Li-ion batteries enabled by completely inorganic electrodecoated silicalite separators, Sustain. Energy Fuels 4 (11) (2020) 5783–5794, https://doi.org/10.1039/d0se01058h.
- [33] D.R.L. Murali, F. Banihashemi, J.Y.S. Lin, Zeolite membrane separators for fire-safe Li-ion batteries – effects of crystal shape and membrane pore structure, J. Memb. Sci. 680 (2023), https://doi.org/10.1016/j.memsci.2023.121743.
- [34] X. Lu, Y. Peng, Z. Wang, Y. Yan, A facile fabrication of highly b-oriented MFI zeolite films in the TEOS-TPAOH-H2O system without additives, Microporous Mesoporous Mater. 230 (2016) 49–57, https://doi.org/10.1016/j. micromeso.2016.04.037.
- [35] S. Ergun, Determination of particle density of crushed porous solids, Anal. Chem. 23 (1951) 151–156, https://doi.org/10.1021/ac60049a031.
- [36] J. Landesfeind, J. Hattendorff, A. Ehrl, W.A. Wall, H.A. Gasteiger, Tortuosity determination of battery electrodes and separators by impedance spectroscopy, J. Electrochem. Soc. 163 (2016) A1373–A1387, https://doi.org/10.1149/ 2.1141607jes.
- [37] J. Wu, M. Fenech, R.F. Webster, R.D. Tilley, N. Sharma, Electron microscopy and its role in advanced lithium-ion battery research, Sustain. Energy Fuels 3 (2019) 1623–1646, https://doi.org/10.1039/C9SE00038K.
- [38] J.C. Lin, M.Z. Yates, Altering the crystal morphology of zeolite-1 through microemulsion-based synthesis, Langmuir 21 (2005) 2117–2120, https://doi.org/ 10.1021/la0473456.
- [39] K. Rafiz, Y. Jin, Y.S. Lin, Performance of electrode-supported silica membrane separators in lithium-ion batteries, Sustain. Energy Fuels 4 (2020) 1254–1264, https://doi.org/10.1039/C9SE00826H.
- [40] J. Motuzas, A. Julbe, R.D. Noble, A. van der Lee, Z.J. Beresnevicius, Rapid synthesis of oriented zeolite-1 membranes by microwave-assisted hydrothermal treatment, Microporous Mesoporous Mater. 92 (2006) 259–269, https://doi.org/10.1016/i.micromeso.2006.01.014.
- [41] E.M. Flanigen, J.M. Bennett, R.W. Grose, J.P. Cohen, R.L. Patton, R.M. Kirchner, J. V. Smith, Zeolite, a new hydrophobic crystalline silica molecular sieve, Nature 271 (1978) 512–516. https://doi.org/10.1038/271512a0.
- [42] (Michael M.J.) M.M.J Treacy, J.B. Higgins, M.M.J. Treacy, International Zeolite Association. Structure Commission, Collection of Simulated XRD Powder Patterns For Zeolites, Elsevier, 2001.
- [43] F. Banihashemi, A. Ibrahim, A. Babaluo, J. Lin, Template-free synthesis of highly boriented MFI-type zeolite thin films by seeded secondary growth, Angew. Chem. Int. Ed. Engl. (2019) 1–6, https://doi.org/10.1002/anie.201814248.
- [44] J. Liu, H. Yuan, X.B. Cheng, W.J. Chen, M. Titirici, J.Q. Huang, T. Yuan, Q. Zhang, A review of naturally derived nanostructured materials for safe lithium metal batteries, Mater. Today Nano 8 (2019), 100049, https://doi.org/10.1016/j. mtnano.2019.100049.
- [45] A. Varzi, K. Thanner, R. Scipioni, D. di Lecce, J. Hassoun, S. Dörfler, H. Altheus, S. Kaskel, C. Prehal, S.A. Freunberger, Current status and future perspectives of lithium metal batteries, J. Power Sources 480 (2020), 228803, https://doi.org/ 10.1016/i.jpowsour.2020.228803.
- [46] S.A. Krachkovskiy1, J.D. Bazak1, S. Fraser1, I.C. Halalay, G.R. Goward, Determination of mass transfer parameters and ionic association of LiPF6: organic carbonates solutions, J. Electrochem. Soc. 4 (2017) 164, https://doi.org/10.1149/ 2.1531704jes
- [47] F. Shen, M.B. Dixit, X. Xiao, K.B. Hatzell, Effect of pore connectivity on Li dendrite propagation within LLZO electrolytes observed with synchrotron X-ray tomography, ACS Energy Lett. 3 (2018) 1056–1061, https://doi.org/10.1021/ acsenergylett.8b00249.
- [48] Y.J. Gong, J.W. Heo, H. Lee, H. Kim, J. Cho, S. Pyo, H. Yun, H. Kim, S.Y. Park, J. Yoo, Y.S. Kim, Nonwoven rGO fiber-aramid separator for high-speed charging and discharging of Li metal anode, Adv. Energy Mater. 10 (2020), 2001479, https://doi.org/10.1002/aenm.202001479.